Pulsed photoacoustic Doppler flowmetry using time-domain cross-correlation: Accuracy, resolution and scalability

Joanna Brunker[a] and Paul Beard
Department of Medical Physics and Bioengineering, University College London, Gower Street, London WC1E 6BT, UK

(Received 2 February 2012; revised 21 June 2012; accepted 27 June 2012)

The feasibility of making spatially resolved measurements of blood velocity using a pulsed photoacoustic Doppler technique in acoustic resolution mode has been investigated. Doppler time shifts were quantified via cross-correlation of photoacoustic waveform pairs generated within a blood-simulating phantom using pairs of light pulses. The phantom comprised micron-scale absorbers imprinted on an acetate sheet and moved at known velocities. The photoacoustic waves were detected using PZT ultrasound transducers operating at center frequencies of 20 MHz, 5 MHz and 3.5 MHz; measurements of velocity and resolution were calculated from the mean cross-correlation function of 25 waveform pairs. Velocities in the range ± 0.15 to $\pm 1.5\,\mathrm{ms}^{-1}$ were quantified with accuracies as low as 1%. The transducer focal beam width determines a maximum measurable velocity $|V_{\max}|$ beyond which correlation is lost due to absorbers moving out of the focal beam between the two laser pulses. Below $|V_{\max}|$ a measurement resolution of $<4\%$ of the measured velocity was achieved. Resolution and $|V_{\max}|$ can be scaled to much lower velocities such as those encountered in microvasculature ($< 50\ \mathrm{mms}^{-1}$). The advantage of pulsed rather than continuous-wave excitation is that spatially resolved velocity measurements can be made, offering the prospect of mapping flow within the microcirculation.
 [http://dx.doi.org/10.1121/1.4739458]

PACS number(s): 43.80.Jz, 43.64.Yp, 43.38.Zp, 43.35.Ud [TDM] Pages: 1780–1791

I. INTRODUCTION

Photoacoustic imaging relies upon the use of laser generated ultrasound to produce optical absorption based images of soft tissues.[1] Endogenous image contrast is dominated by hemoglobin on account of its strong optical absorption at visible and near infrared wavelengths. As a consequence, photoacoustic imaging is well suited to providing images of vascular anatomy.[2–4] In addition, by varying the excitation laser wavelength and exploiting the known spectral differences between oxy- and deoxy-hemoglobin, measurements of absolute blood oxygen saturation can be made.[5] This ability to characterize the structure and oxygenation status of the vasculature makes the technique well suited to the study of tumors and other pathologies characterized by abnormalities in perfusion and oxygen supply. A further potential functional capability is the measurement of blood velocity using Doppler flowmetry techniques. This would be useful in its own right, for example to study flow in tumor vessels where the tortuous nature of the microvasculature can lead to chaotic and variable blood flow which can inhibit therapeutic response. However, if both blood flow and oxygen saturation can be measured simultaneously there is also the prospect of being able to estimate oxygen delivery and thus provide a measure of oxygen consumption—an important physiological parameter that is almost impossible to measure non-invasively using other methods without employing contrast agents. Photoacoustic flow measurements can be made in a manner analogous to conventional pulse echo Doppler ultrasound—that is to say by recovering the Doppler frequency, phase or time shift encoded on to photoacoustic waves emitted by moving red blood cells. Unlike Doppler ultrasound, however, the detected acoustic signal is emitted by the blood cells as opposed to being weakly reflected from them. This offers significant SNR advantages especially when measuring flow in microvessels as these exhibit low echogenicity. Furthermore, Doppler ultrasound measurements of the relatively low flow velocity ($< 50\ \mathrm{mms}^{-1}$) in microvessels can be corrupted by the much larger backscattered signal from the surrounding tissue which can move at comparable speeds due to respiratory or cardiac motion. In photoacoustic Doppler flowmetry this is likely to be less problematic due to the strong optical absorption of blood compared to that of the vessel wall and surrounding tissue. For these reasons, photoacoustic Doppler is envisaged primarily for the measurement of the low flow velocities in the microvasculature, not fast moving blood in the major arteries which is currently well served by conventional pulsed wave Doppler ultrasound.

The basic principles of photoacoustic Doppler flowmetry were first outlined over a decade ago.[6] Subsequently, photoacoustic measurements of flow in a tissue mimicking phantom were obtained by recovering Doppler frequency shifts using CW excitation.[7] However, in common with CW Doppler ultrasound, this approach cannot readily provide depth-resolved measurements. The use of pulsed excitation overcomes this limitation and with this in mind a number of signal processing schemes have now been demonstrated. Sheinfeld *et al.* describe a frequency-domain method that employs narrowband toneburst excitation and a spectral analysis of the resulting photoacoustic waves in order to recover the Doppler frequency shifts. As with most spatially

[a]Author to whom correspondence should be addressed. Electronic mail: joanna.brunker.09@ucl.ac.uk

resolved Doppler flowmetry schemes, there is inevitably a velocity-spatial resolution compromise. For example, in one study,[8] a long toneburst duration of 3 μs was used providing a velocity resolution of 1.5 mms^{-1} but a relatively low depth resolution of 4.5 mm. Moreover, although this study used light in the wavelength range of 1530–1565 nm to demonstrate the concept in a phantom, the limited availability of quasi-CW-modulated laser sources with sufficient output power at wavelengths that provide adequate penetration depth in tissue (i.e., wavelengths <900 nm) may present a practical limitation. Yao *et al.*[9] describe a pulsed time-domain approach for estimating the acoustic bandwidth broadening arising from the frequency difference between the extremities of a wavefront emitted by a target moving orthogonal to the axis of a focused transducer. This approach relies upon delivering a number of laser pulses to the tissue and recording the motion-induced fluctuations in the magnitude of the corresponding photoacoustic waveforms at a specific point in their time records. This discretely sampled time varying signal can then be used to estimate the velocity by computing its autocorrelation function in a manner analogous to autocorrelation based velocity estimation methods employed in color flow ultrasound imaging.[10,11] This approach has successfully been used to measure blood flow with sub-mm/s velocity resolution in the microvasculature *in vivo* and also combined with measurements of other physiological parameters (including oxygen saturation) to give an estimate of the rate of oxygen consumption.[12] However, it was achieved by deploying the "optical resolution" mode of photoacoustic sensing. This relies on using a focused laser beam to laterally localize the signal and is limited to a maximum penetration depth of approximately 1 mm due to the resolution degrading effects of the strong optical scattering exhibited by tissue. The method has yet to be demonstrated using the more general mode of photoacoustic sensing in which localization is acoustically defined and which provides much greater penetration depths. A variant of the above method, so-called photoacoustic correlation spectroscopy, has also been demonstrated *in vivo*,[13] again in optical resolution mode. This approach exploits the velocity dependent decay in photoacoustic signal amplitude that occurs as a group of absorbers moves across the field-of-view of the ultrasound receiver.

In this paper, we describe a different Doppler flowmetry approach, which is based upon time correlation signal processing. This method is inspired by time correlation ultrasound flowmetry[14,15] and relies upon measuring the change in the time-of-arrival of successive photoacoustic waves emitted by a moving cluster of red blood cells under pulsed excitation using the cross-correlation function. It has the advantage that, by using short (nanosecond) laser pulses, it offers depth-resolved measurements with high spatial resolution and can employ the type of readily available pulsed Q-switched lasers used routinely in photoacoustic tissue imaging. It is also an inherently flexible approach. Velocity range and resolution are scalable with excitation pulse separation allowing it be optimized for a wide range of physiologically realistic flow velocities. It also lends itself to both the acoustic and optical resolution modes of photoacoustic sensing enabling measurements to be made over the spatial scales of both modes. Preliminary measurements in phantoms have been reported previously.[16,17] In this paper we provide a detailed account of the underlying methodology, experimental technique, signal processing scheme and error analysis. Section II describes the underlying principles of the technique and Sec. III the experimental methods employed to evaluate it. Section IV discusses the signal processing methods used to estimate the velocity from the measured photoacoustic waveforms. The experimentally determined velocity measurements, resolution and dynamic range are presented and discussed in Sec. V.

II. PRINCIPLES OF PULSED PHOTOACOUSTIC DOPPLER FLOWMETRY

Figure 1 shows a schematic that illustrates the concept. A sample of tissue is irradiated with a wide field pulsed laser beam. Photoacoustic waves are emitted predominantly by the red blood cells (RBCs) within a subsurface blood vessel and detected by a directional ultrasound detector located on the tissue surface. Since an extended region of the tissue is illuminated due to the diffuse nature of light transport in tissue, the dimensions of the focal beam of the detector, rather than the illuminated volume, define the region over which the signals are collected and hence the lateral spatial resolution—the so-called acoustic resolution mode of photoacoustics. This is in contrast to previous flowmetry methods,[9,13,18] which employ the optical resolution mode of photoacoustic microscopy and are thereby limited to sub-millimeter penetration depths.

In order to measure the flow of blood within a vessel as depicted in Fig. 1, two assumptions about the spatial heterogeneity of blood are made. Firstly, that it is composed of an ensemble of randomly distributed clusters of RBCs and secondly that the density and orientation of RBCs within each cluster is also random. Thus, when irradiated with a laser pulse, a given cluster will emit a unique photoacoustic signature. By delivering a train of laser pulses and recording this signature over time, the motion of the cluster can be tracked at discrete time intervals as it progresses along the vessel. In its simplest form, this requires using two laser pulses, separated by a time T, to acquire a pair of photoacoustic waveforms that are identical in shape but shifted in time with respect to each other due to the motion of the RBC cluster. By cross-correlating these waveforms, the time shift between them can be obtained in order to estimate the velocity. In practice, this is achieved by delivering the first laser pulse, recording the resulting photoacoustic waveform and selecting a short time segment $p_1(t)$ that corresponds to the depth at which the blood vessel lies. The length of the time segment is proportional to the length D—the range gate—which determines the axial spatial resolution. The second laser pulse is emitted at a time T later during which the RBC cluster will have moved along the vessel thus altering the distance the photoacoustic waves will have travelled to the detector. The detected signal $p_2(t)$ due to the second laser pulse will therefore be a time-shifted replica of the first, assuming that during time T the RBC cluster has neither

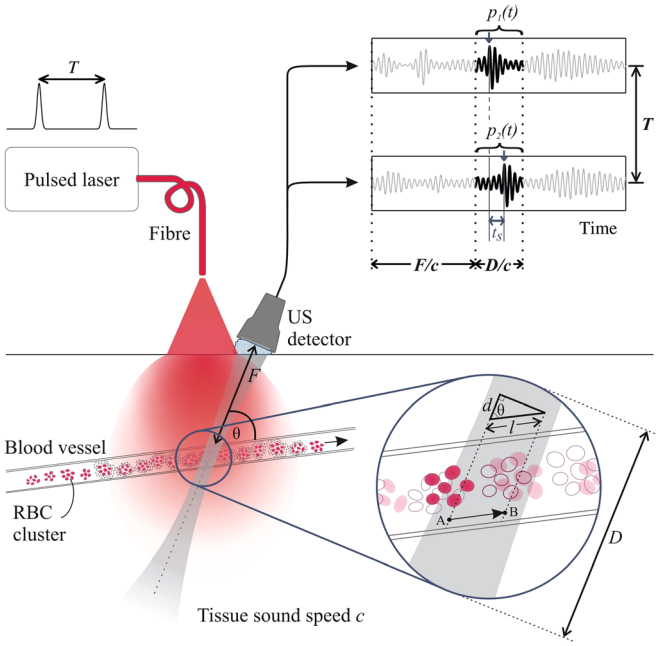

FIG. 1. (Color online) Schematic showing the detection of time-shifted photoacoustic signals. The two signals are generated from clusters of moving red blood cells (RBCs) when illuminated by a pair of laser pulses separated by a time T. The inset shows the distribution of RBCs (represented by solid ellipses) when the first laser pulse is fired, and the new positions (unfilled ellipses) coincident with the firing of the second laser pulse a time T later. Between the two pulses the cells have moved from A to B, a distance l along the blood vessel. The waveforms show segments of the two photoacoustic signals $p_1(t)$ and $p_2(t)$ that correspond to the location of the blood vessel and illustrate the time shift t_s between the two due to the motion of the RBCs.

completely moved out of the focal beam of the detector nor undergone significant changes in its geometry or density which would alter its photoacoustic signature. In other words, the two signals must not have become completely decorrelated over time T. The velocity is then obtained from the time shift t_s between $p_1(t)$ and $p_2(t)$ as follows:

$$t_s = \frac{d}{c}, \tag{1}$$

where $d = l\cos\theta$ is the distance the RBC cluster has moved in the direction of a vector connecting the sample volume to the receiver, c is the speed of sound in the medium and θ is the angle between the direction of motion and the axis of the transducer receive beam. The velocity V of the RBC cluster is given by

$$V = \frac{l}{T}, \tag{2}$$

which, using Eq. (1), can then be written

$$V = \frac{ct_s}{T\cos\theta}. \tag{3}$$

This is analogous to the classical Doppler frequency equation derived for a moving sound source except that the velocity is now proportional to a fractional time shift rather than a fractional frequency shift.

The cross-correlation function can be used to determine the time shift t_s between the two photoacoustic waveforms $p_1(t)$ and $p_2(t)$. For continuous functions the cross-correlation is defined as:

$$(p_1 \star p_2)(t) = \int_{-\infty}^{\infty} p_1^*(\tau)p_2(t+\tau)d\tau, \tag{4}$$

where p_1^* is the complex conjugate of p_1.

Discretely sampled signals $\mathbf{p_{kn}}(\mathbf{k} = 1, 2)$ are related to their continuous counterparts as follows:

$$\mathbf{p_{kn}} \equiv p_k(t)|_{t=n\Delta t} \tag{5}$$

for sample spacing Δt, and where $n = 0, \ldots, N-1$. For these discrete N-length vectors, an estimate of the cross-correlation function is given by

$$\hat{R}_{\mathbf{p_1p_2}}(m) = \begin{cases} \dfrac{1}{N-|m|}\displaystyle\sum_{n=0}^{N-m-1} \mathbf{p}_{1(n+m)}\mathbf{p}_{2n}^* & m \geq 0 \\ \hat{R}_{\mathbf{p_2p_1}}^*(-m) & m < 0. \end{cases} \tag{6}$$

The normalization factor $1/(N-|m|)$ produces an output vector $c(m) = \hat{R}(m-N)$, $m = 1, \ldots, 2N-1$, that is unbiased, avoiding the zero bias inherent in the standard cross-correlation function.[19]

Although for illustrative purposes, only a single blood vessel is shown in Fig. 1, in reality, there will be a number of vessels at different depths within the detector field-of-view. The blood flow in each of these can be ascertained by advancing the range gate along the time records of the two photoacoustic waveforms, computing the cross-correlation at each temporal position to obtain the time shift and using Eq. (3) to obtain V. In this way a depth profile of velocity along the transducer line-of-sight can be obtained revealing flow wherever it is present.

III. EXPERIMENTAL METHOD

Figure 2 shows the experimental setup used to demonstrate the technique. A phantom comprising micron-scale absorbers imprinted on a rotating disc was used to simulate the motion of red blood cells. A region of the phantom was excited with pairs of laser pulses separated by time T. Light absorbing particles within the target area emitted a photoacoustic wave each time they were illuminated and these waves were detected using an ultrasound transducer and acquired using an oscilloscope.

The phantom comprises a Perspex disc mounted on the axle of a DC electric motor the speed of which was continuously adjustable. The disc is overlaid with a sheet of acetate imprinted around its rim with a non-uniform, random pattern of light-absorbing micron-scale dots. Illumination of a region (about 2 cm in diameter) near the edge of the disc allowed the rotary motion of the dots ("particles") to be approximated to the linear flow of red blood cell clusters. The diameter of the illuminated region was chosen so that it was always significantly larger than the diameter of the

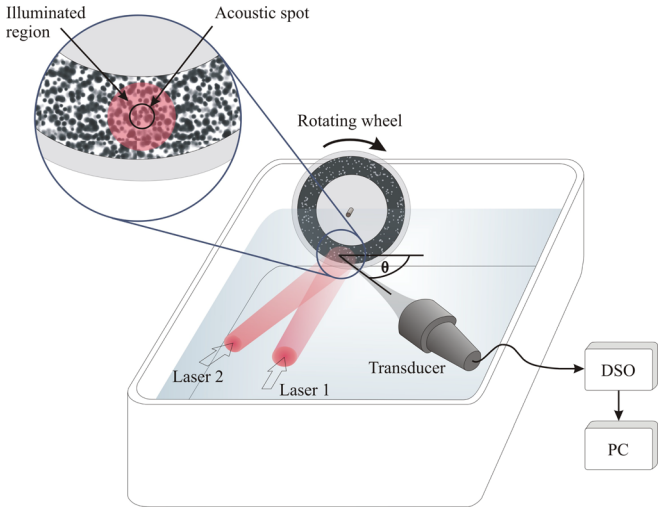

FIG. 2. (Color online) Experimental setup for pulsed photoacoustic Doppler flow measurement where the motion of micron-scale absorbers imprinted on to the rim of a rotating wheel is used to represent blood flow. Two laser pulses (one emitted by laser 1 and the other by laser 2) separated by a time T are used to generate a pair of acoustic waveforms which are detected by an ultrasound receiver. The inset shows a typical distribution of the micron-scale dots printed onto the wheel phantom. A large area (at least 2 cm diameter) of the absorbers is illuminated, but photoacoustic signals are only collected from the smaller region defined by the transducer focal spot. The signals were captured by an oscilloscope (DSO) and downloaded to a PC.

detector focal beam in order to be representative of the acoustic resolution mode of photoacoustic detection.

The distribution of the absorbing dots is shown in Fig. 3. The typical dimensions of the dots are on the order of 10 μm and they cover approximately 90% of the total imprinted area. This is comparable to the diameter and volume fraction of red blood cells which are on average 7.5 μm[20,21] and about 50%, respectively.

Photoacoustic waveform pairs were generated using pairs of laser pulses with pulse separations T in the range 0.1 ms to 50 ms. Two Q-switched Nd:YAG lasers emitting at 1064 nm were used to produce the pulse pairs. The lasers were triggered using a counter/timer programmed with a DAQ card (NI PCI-6024E) to give a pre-selected time delay T. The beams emitted by each laser were adjusted to be of the same diameter and carefully aligned so that they irradiated exactly the same region of the phantom. Note that two lasers were used solely to demonstrate the concept in the first instance. A single laser that could provide the necessary pulse separations could be employed and indeed would be preferable to avoid alignment errors and reduce the complexity of the system.

The photoacoustic signals were detected using a PZT transducer. Three different transducers were used variously in this study. One was a planar transducer with a center frequency of 20 MHz (beam width $\approx$ 1.28 mm). The remaining two were focused transducers, one with a center frequency of 5 MHz and a spherical focus (focal length: 63 mm; focal beam width: 0.97 mm), and the other with a center frequency of 3.5 MHz and a cylindrical focus (focal length: 32 mm; focal beam width: 1.98 mm). The transducer position and angle θ were adjusted to give the maximum photoacoustic signal; for the focused transducers this involved setting the

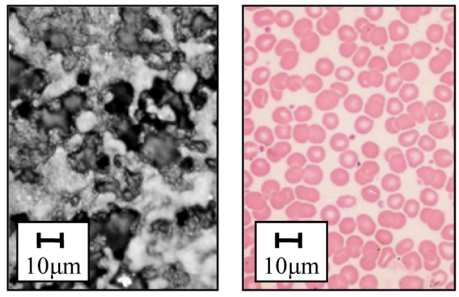

FIG. 3. (Color online) Comparison of optical microscopy images showing the distribution of absorbers in the phantom (left) and a histological section (Ref. 20) containing red blood cells (right). The scale bars are only approximate, but it is clear that the "particle" dimensions and densities in both images are comparable. In the phantom the "particles" comprise micron-scale dots printed onto an acetate sheet.

distance from the illuminated region of the wheel to be approximately equal to the transducer focal length. The angle θ was measured to the nearest degree using a turntable with angular markings at 1° intervals.

Measurements of velocity V' (see Sec. IV) were made for different wheel speeds in order to determine the capability of the technique for estimating velocities within the range $\pm 0.15\,\mathrm{ms}^{-1}$ to $\pm 1.5\,\mathrm{ms}^{-1}$. Measurements were limited to this range because below $0.15\,\mathrm{ms}^{-1}$ the speed of the motor was non-uniform, and above $1.5\,\mathrm{ms}^{-1}$ turbulence in the water bath distorted the measured signal. The angular velocity of the wheel phantom was measured by using the spokes of a wheel mounted behind the Perspex disc to form a chopper that periodically intercepted a beam of light between an LED and a photodiode. Calculation of the linear velocity from the angular velocity required measurement of the radial distance R from the wheel center to the center of the focal region of the transducer. Uncertainties in the linear velocity were estimated from the variation in the angular velocity measured by the chopper over a single revolution and the uncertainty in the measurement of R. The velocity values obtained using this method were regarded as the "known" values V and compared with those acquired via cross-correlation of the photoacoustic waveform pairs (V').

IV. SIGNAL ACQUISITION AND PROCESSING

To obtain a single velocity estimate, the phantom was irradiated by a train of 25 laser pulse pairs. The pulses within each pair are separated by a time T which is typically between 0.1 ms and 10 ms depending on the velocity range being measured. Each pulse pair was separated by 50 ms limited by the 20 Hz maximum PRF of the lasers used—a higher PRF would permit much faster acquisition, with the minimum pulse pair separation ultimately limited by the acoustic transit time from the maximum depth of interest to the detector (which for cm depths is of the order of tens of microseconds). The corresponding photoacoustic waveform pairs produced by the laser pulse train were captured using the FastFrame™ Segmented Memory feature of the oscilloscope (DSO-Tektronix TDS784D). This enabled all 25 photoacoustic waveform pairs to be acquired in real time, concatenated in a single record and downloaded to a PC. Figure 4(a)

shows an example of one such FastFrame record and Fig. 4(b) shows a single waveform pair extracted from this record – this data was obtained with the phantom moving at a velocity of $0.13 \pm 0.02\,\mathrm{ms}^{-1}$, with $T = 1$ ms and using the 5 MHz focused transducer. Figure 4(c) shows normalized versions of the two waveforms superimposed on the same graph in order to illustrate the time shift t_s between them. The discrete unbiased cross-correlation function [Eq. (6)] was then evaluated as illustrated in Fig. 4(d). The time shift t_s between the waveform pair is then given by the horizontal position of the peak value of the cross-correlation function.

To obtain a velocity estimate, the cross-correlation functions of all 25 waveform pairs in Fig. 4(a) were computed and normalized to their maximum amplitudes. The normalized cross-correlation functions were then averaged to obtain a mean cross-correlation function $C(t)$ which is shown in Fig. 5(a). The standard deviation δy_i, which represents the uncertainty in the magnitude of each data point in Fig. 5(a), was also calculated although it is not shown in the figure. The central lobe of $C(t)$ was then extracted [the m data points between the vertical dotted lines in Fig. 5(a)] and a continuous function $g(t)$ fitted to it: in this example $g(t)$ is a Gaussian as shown in Fig. 5(b). The horizontal position of the peak value of the fit was taken to be the time shift t_s' from which the velocity value V' was calculated using Eq. (3).

The uncertainty $\Delta t_s'$ in the measured time shift t_s' is given by the uncertainty in the location of the peak value of $C(t)$. This was estimated from the standard deviation values (the y axis error bars δy_i) of the data points associated with the central lobe as follows. At each of the time shift data points t_i a sensitivity value s_i was calculated by numerical differentiation of the fitted curve:

$$s_i = \left|\frac{dg_i}{dt_i}\right|. \tag{7}$$

Time shift (x axis) errors δt_i for each point were then obtained from δy_i as follows:

$$\delta t_i = \frac{\delta y_i}{s_i}. \tag{8}$$

$\Delta t_s'$ was then taken as the mean of the x axis errors δt_i, weighted according to the sensitivities s_i:

$$\Delta t_s' = \frac{\sum_{i=1}^{m}(s_i \cdot \delta t_i)}{\sum_{i=1}^{m} s_i}. \tag{9}$$

The corresponding uncertainty $\pm\Delta V'/2$ in the velocity V' was then calculated using Eq. (3):

$$\frac{\Delta V'}{2} = \frac{c}{T\cos\theta}\frac{\Delta t_s'}{2}. \tag{10}$$

This assumes that the relative uncertainties for the sound speed c, the pulse separation T and the angle θ are negligible compared to the relative uncertainty $\Delta t_s'/t_s'$ in the time shift. For the data shown in Fig. 5(b) the peak of the Gaussian fit

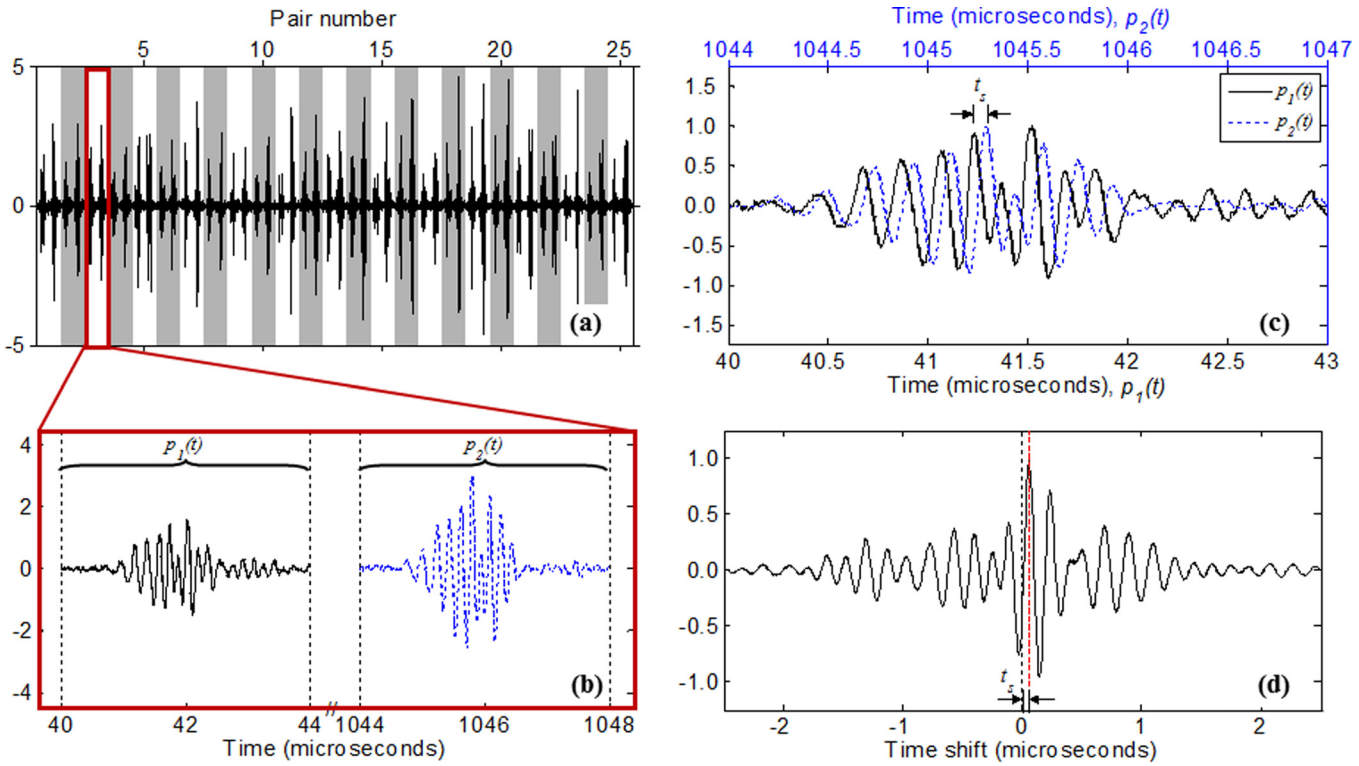

FIG. 4. (Color online) Signal processing scheme used to estimate time shift. (a) A FastFrame record consisting of 25 waveform pairs. Each pair of photoacoustic waveforms was acquired using a 5 MHz focused transducer following double pulse illumination ($T = 1$ ms) of the rotating wheel phantom. One such pair is enlarged in (b) where the first waveform $p_1(t)$ and second waveform $p_2(t)$ in the pair are shown in solid and dashed lines, respectively. The two waveforms are overlaid and normalized in (c) in order to illustrate the time shift t_s between them. The lower plot in (d) shows the cross-correlation function corresponding to the waveform pair. The position of the peak is marked with a dashed line and corresponds to the time shift t_s.

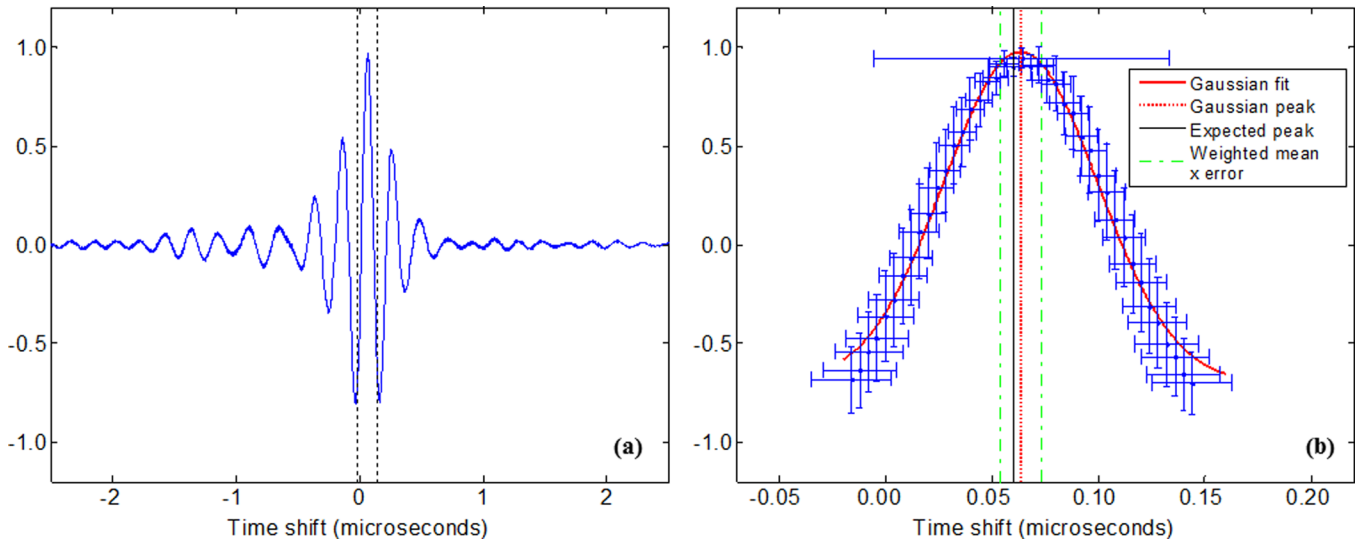

FIG. 5. (Color online) (a) Mean cross-correlation function of the 25 photoacoustic waveform pairs shown in Fig. 4(a). (b) Expanded view of data between the vertical dotted lines in (a). For each data point, the y axis error bars correspond to the standard deviation of the 25 cross-correlation functions, and, using the Gaussian fit (solid curve), these errors are propagated to time shift (x axis) errors. The weighted mean time shift error is calculated using Eq. (9) and indicated by the dashed vertical lines either side of the peak of the Gaussian fit (vertical dotted line). The solid vertical line marks the position of the peak corresponding to the known velocity V.

and the error calculated [using Eq. (10)] gives a measured velocity of $0.14 \pm 0.01\,\mathrm{ms}^{-1}$, which is in good agreement with the known value ($0.13 \pm 0.02\,\mathrm{ms}^{-1}$) within the experimental uncertainty.

V. RESULTS

To demonstrate the concept, measurements were made for velocities in the range $|V| = 0.15 - 1.5\,\mathrm{ms}^{-1}$ using three different transducers: 20 MHz planar, 5 MHz spherical focused and 3.5 MHz cylindrical focused. The results are shown in Fig. 6. These data demonstrate that the majority of the photoacoustically measured velocities are in close agreement with the known values, the former increasing linearly with the latter. Although a detailed error analysis is provided in the following sub-sections, a cursory inspection of Fig. 6 permits several observations in relation to the accuracy and resolution of the measurements to be made. Consider the results in Fig. 6(a) acquired using the 20 MHz planar transducer. In the range $|V| = 0.15 - 1.0\,\mathrm{ms}^{-1}$, the measurements are consistently accurate to within 3% of the known velocities. The measurement resolution (vertical error bars) is on average about 6% of the measured velocity over the same velocity range, but approaches 10% for velocities approaching $|V| = 1.1\,\mathrm{ms}^{-1}$. This is due to a reduction in correlation between the measured waveforms pairs as the distance the absorbers travel between successive laser pulses approaches that of the transducer focal beam width. At even higher velocities the absorbers move completely out of the transducer field-of-view between the two laser pulses resulting in near-complete loss of correlation and nonsensical velocity estimates—this defines the maximum measurable velocity, $|V_{\max}|$. Similar behavior is observed for the measurements made using the 5 MHz focused transducer [Fig. 6(b)], although $|V_{\max}|$ is lower because of the smaller transducer focal spot size. For the 3.5 MHz cylindrically focused transducer [Fig. 6(c)] the measurements do not reach a limiting value within the range of velocities investigated due to the larger transducer beam width. Since all three data sets were recorded under identical experimental conditions, the differences in maximum measurable velocity, accuracy and resolution are due to the individual transducer characteristics.

The following three sub-sections discuss in more detail the factors that influence (a) the maximum measurable velocity, (b) the accuracy, and (c) the resolution of the measurements. The fourth sub-section describes how the results can be scaled to estimate the measurement resolution and the upper velocity limit for different velocity ranges. The final sub-section discusses how the velocity resolution is affected by the axial spatial resolution.

A. Upper velocity limits

The results in Figs. 6(a) and 6(b) show that there are threshold velocities $|V_{\max}| \cong 1.1\,\mathrm{ms}^{-1}$ and $|V_{\max}| \cong 0.8\,\mathrm{ms}^{-1}$, respectively beyond which the estimated velocity drops off very rapidly and bears little relation to the true velocity. This occurs because the irradiated absorbers have been swept entirely out of the transducer focal beam by the time the second laser pulse is emitted. As a consequence, there is almost a complete loss of correlation between the two waveforms within each pair. This effect is not observed in Fig. 6(c) due to the larger beam width of the 3.5 MHz cylindrically focused transducer; this increases $|V_{\max}|$ to over $1.8\,\mathrm{ms}^{-1}$, which is beyond the range of measured velocities.

A theoretical value for the threshold or limiting speed $|V_{\max}|$ (meters per second) can be calculated from the focal beam diameter w and the pulse separation T:

$$|V_{\max}| = \frac{w_p}{T} = \frac{w}{T|\sin\theta|}, \tag{11}$$

w is defined as the FWHM beam width at the focal length of the transducer, and the geometrical relationship between w and w_p is illustrated in Fig. 7.

From Eq. (11) it can be seen that $|V_{max}|$ depends on the pulse separation T as well as the beam width w. This behavior is shown in Fig. 8. Measurements in the range 0–1.5 ms^{-1} were made using the 5 MHz focused transducer and laser pulse separations between 1.2 ms and 6 ms, and the observed cut-off velocity is plotted as a function of time separation between the laser pulses. The maximum measurable velocity varies inversely with the pulse separation, and the data agree almost exactly with the theoretical values (solid line) calculated from Eq. (11); the known beam width w of the transducer was 0.97 mm as determined by mapping the beam profile of the transducer when operating it as a transmitter.

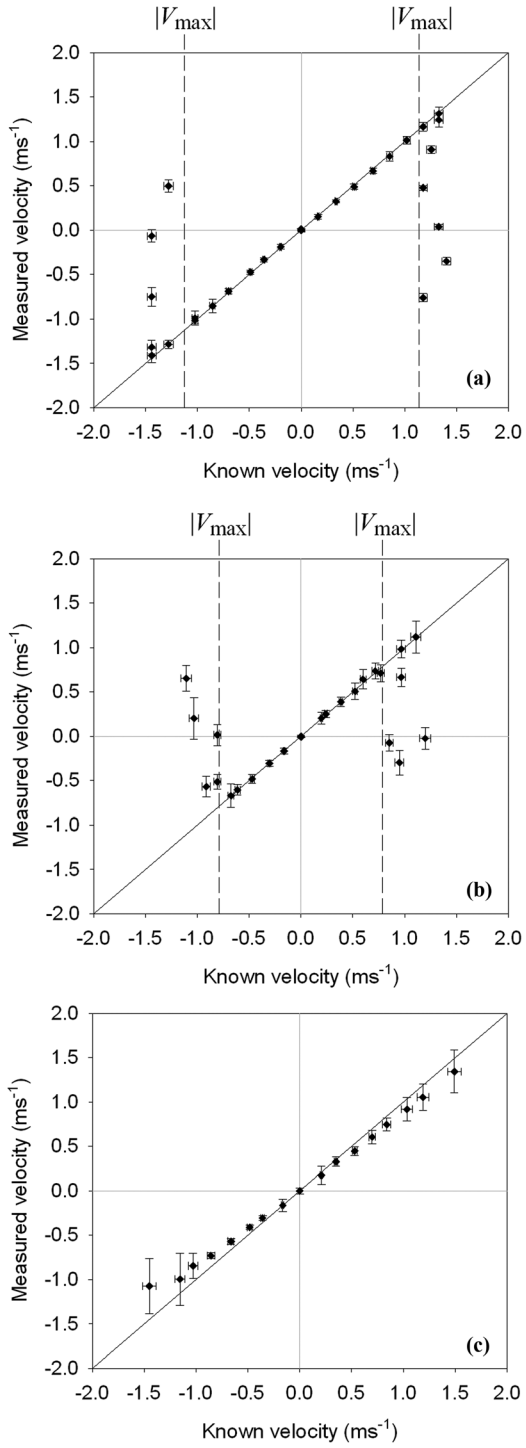

FIG. 6. Comparison of velocity values V' calculated from the time-shifted photoacoustic waveform pairs with the known velocities V of the absorbers in the rotating wheel phantom. The time separation between the laser pulses was 1.5 ms. The data in (a) were acquired using a 20 MHz planar transducer with $\theta = 48°$, in (b) using a 5 MHz focused transducer with $\theta = 45°$, and in (c) using a 3.5 MHz cylindrically focused transducer with $\theta = 48°$. Correlation is lost for velocities beyond that marked by the dashed lines. The solid lines are lines of unity.

A large transducer beam width and a short laser pulse separation both conspire to increase $|V_{max}|$. Selection of appropriate w_p and T therefore allows control over the maximum measurable velocity. Similarly, for measurement of a particular velocity V there exists a maximum pulse separation T_{max} beyond which V can no longer be accurately measured. Thus, for a specific velocity V and beam diameter w Eq. (11) can be re-expressed:

$$T_{max} = \frac{w_p}{|V|} = \frac{w}{|V \sin\theta|}. \tag{12}$$

Since the time shift t_s is proportional to both the speed $|V|$ and the pulse separation T, a maximum measurable time shift $t_{s,max}$ can be found by rearranging Eq. (11) or Eq. (12) and substituting Eq. (3):

$$t_{s,max} = \frac{w}{c|\tan\theta|}. \tag{13}$$

B. Velocity accuracy

The accuracy of the velocity measurements is described by the fractional difference between the known velocity (V) and measured value (V'):

$$\text{Fractional error} = \frac{V - V'}{V} \quad (V \neq 0). \tag{14}$$

Figure 9 illustrates the accuracy of the measurements made using the 3.5 MHz, 5 MHz, and 20 MHz transducers. The x axis data have been re-scaled to give the velocity as a proportion of the $|V_{max}|$ values calculated for the three transducers so that the limiting velocities of each can be directly compared.

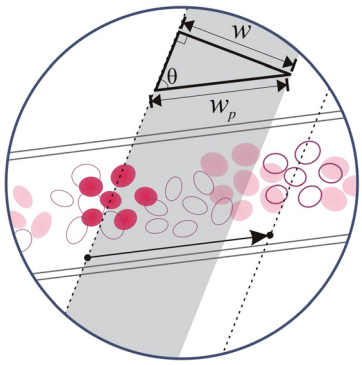

FIG. 7. (Color online) Demonstration of de-correlation due to the finite transducer beam width. If a cluster of RBCs (represented by solid ellipses) moves out of the transducer focal beam (grey shading) in the time between the two laser pulses the velocity is greater than V_{max} and there is no correlation.

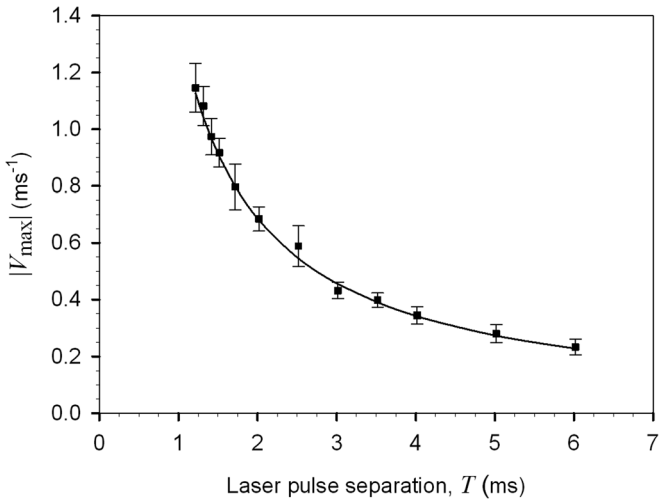

FIG. 8. Values of maximum measurable velocity V_{max} observed using different laser pulse separations T between 1.2 ms and 6.0 ms. The data were acquired using the 5 MHz focused transducer with $\theta = 45°$. The solid line shows the theoretical values of V_{max} calculated using Eq. (11) and the known beam width $w = 0.97$ mm.

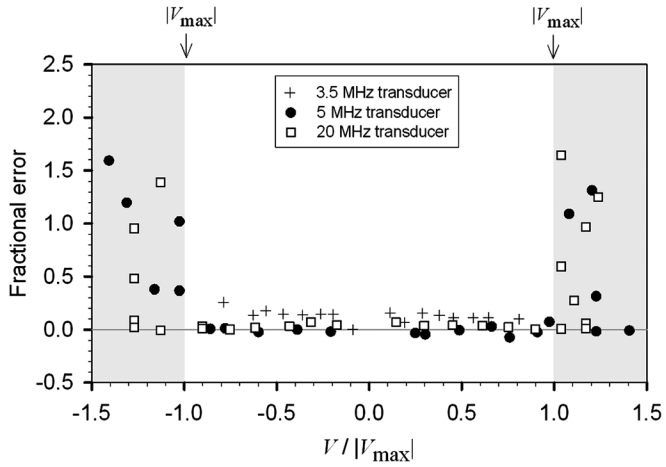

FIG. 9. Accuracy of the data shown in Figs. 6(a)–6(c). For the data acquired using the 5 MHz and 20 MHz transducers, correlation is lost when $V/V_{max} > 1$, giving rise to poor accuracy (large fractional errors, shaded region). The measured range of velocities did not extend beyond V_{max} for the 3.5 MHz transducer.

In general, there is a small and relatively consistent fractional error for measurements made at velocities $|V/V_{max}| < 1.0$: the fractional error averages 3% for the 20 MHz transducer, −1% for the 5 MHz transducer and 13% for the 3.5 MHz transducer. The relatively large underreading (positive error) for the 3.5 MHz transducer is likely to be due to an overestimate of R, the radial distance between the region of focus and the wheel axle.

The regime where $|V/V_{max}| > 1.0$ is only pertinent to the 5 MHz and 20 MHz transducers, for which the fractional errors average 72% and 55%, respectively. $|V_{max}|$ indicates a limit beyond which there is near-complete de-correlation between the two waveforms as a consequence of the absorbers being swept out of the detector field-of-view between successive laser pulses, as discussed in the previous subsection. It might be expected that de-correlation would give rise to a random distribution of velocity measurements; whilst Fig. 6 and Fig. 9 suggest that this is the case to some extent, it is also evident that beyond $|V_{max}|$ the measurements consistently under-read the known velocity values with a tendency towards zero velocities. This is likely to be due to the limited transducer bandwidth, which gives rise to time-shift-independent signal features and therefore an apparent zero time shift between two de-correlated waveforms.

Figure 9 also shows instances of good correlation (fractional error close to zero) still occurring at velocities greater than $|V_{max}|$; this reflects the fact that the transducer beam profile is not a top-hat function, and therefore there is still some possibility that correlation will occur even once the absorbers have moved out of the immediate field-of-view defined by the FWHM. The larger beam width of the 3.5 MHz transducer, when used with the same pulse separation ($T = 1.5$ ms), means that $|V_{max}|$ was beyond the range of measured velocities, and so no large changes are observed in the fractional error.

C. Velocity resolution

The measurement resolution describes the minimum measurable velocity under the experimental conditions described. Ultimately, the smallest detectable time shift δt_s is limited by the temporal sampling interval of the oscilloscope, and is therefore independent of the velocity V and the pulse separation T. For fixed values of c, θ and T, the fundamental velocity resolution limit $\pm \delta V/2$ is proportional to the time sampling interval $\pm \delta t_s/2$ [Eq. (3)]:

$$\frac{\delta V}{2} = \frac{c}{T\cos\theta}\frac{\delta t_s}{2}. \tag{15}$$

The percentage resolution may also be defined as:

$$\frac{\delta V/2}{V} \times 100 = \frac{\delta t_s/2}{t_s} \times 100. \tag{16}$$

Experimental percentage resolution values can be similarly defined using $\pm \Delta t_s'/2$ and $\pm \Delta V'/2$, the uncertainties in the measured time shift t_s' [Eq. (9)] and the measured velocity V' [Eq. (10)].

In order to verify the influence of pulse separation on measurement resolution, a series of measurements was made using signals sampled with $\delta t_s = 4$ ns under experimental conditions where $c = 1476\ \mathrm{ms}^{-1}$ and $\theta = 45°$. The pulse separation was varied in the range 0.1 to 45 ms, and the theoretical measurement resolution $\pm \delta t_s/2$ was compared with the experimentally determined measurement resolution $\pm \Delta t_s'/2$ [Eq. (9)]. The results are shown in Fig. 10 and illustrate three scenarios: $V = 0.00\ \mathrm{ms}^{-1}$, $V = 0.30\ \mathrm{ms}^{-1}$ and $V = 0.77\ \mathrm{ms}^{-1}$. In the case of zero velocity there is no correlation loss due to movement of absorbers out of the transducer focal beam, and therefore these measurements serve as control data. Figure 10(a) shows the absolute resolution values, Fig. 10(b) shows the percentage resolution values and Fig. 10(c) shows the cross-correlation amplitude—the maximum amplitude of the mean cross-correlation functions $C(t)$ (see Sec. IV). The

cross-correlation amplitude provides an approximate measure for the degree of correlation. Note that the x axis data for the moving phantoms have been re-scaled to give the T as a proportion of the T_{max} values calculated for each velocity [Eq. (12)] so that the results can be compared directly.

In the case where the phantom was held stationary, changes in the measurement resolution are due solely to changes in pulse separation: there is no change in the degree of correlation as evidenced by Fig. 10(c) which shows that the cross-correlation amplitude remains close to unity across the range of pulse separations. Figure 10(a) shows that, for $V = 0.00\,\mathrm{ms}^{-1}$, the measurement resolution is independent of T, as expected, but is up to three times the fundamental limit at each pulse separation value. This deviation from the ideal may be due to factors such as fluctuations in laser pulse energy, timing jitter in the synchronization of the two lasers and spurious absorbers moving in the water.

For the moving phantom, the measurement resolution depends not only on the laser pulse separation, but also on the velocity, and therefore the degree of correlation. Figures 10(a) and 10(b) show that, at low pulse separations $T/T_{max} < 0.5$ (indicated with the darkest shading), the absolute resolution is again fairly consistent, but poorer than for the stationary phantom due to reduced correlation, which is exacerbated by irregularity in the wheel motion. The percentage resolution increases in proportion to $1/T$ as the time shift becomes larger compared to the time sampling interval δt_s, as expected. There is a consistently high degree of correlation over this range of pulse separations ($T/T_{max} < 0.5$), as illustrated in Fig. 10(c), although it is evident that even for these small time shifts there is a reduction in the cross-correlation amplitude compared to the stationary case. As the pulse separation is increased further ($0.5 < T/T_{max} < 1$, lighter shading) both the measurement resolution and the cross-correlation amplitude deteriorate due to de-correlation between waveforms in each pair. This de-correlation marks the approach towards the limiting pulse separation T_{max} [Eq. (12)], during which there is a progressive increase in the fraction of illuminated absorbers that move out of the transducer focal beam between the two laser pulses. For measurements exceeding T_{max}, the near-total de-correlation of the waveform pairs means that measurement resolution is no longer dependent on velocity, or indeed pulse separation.

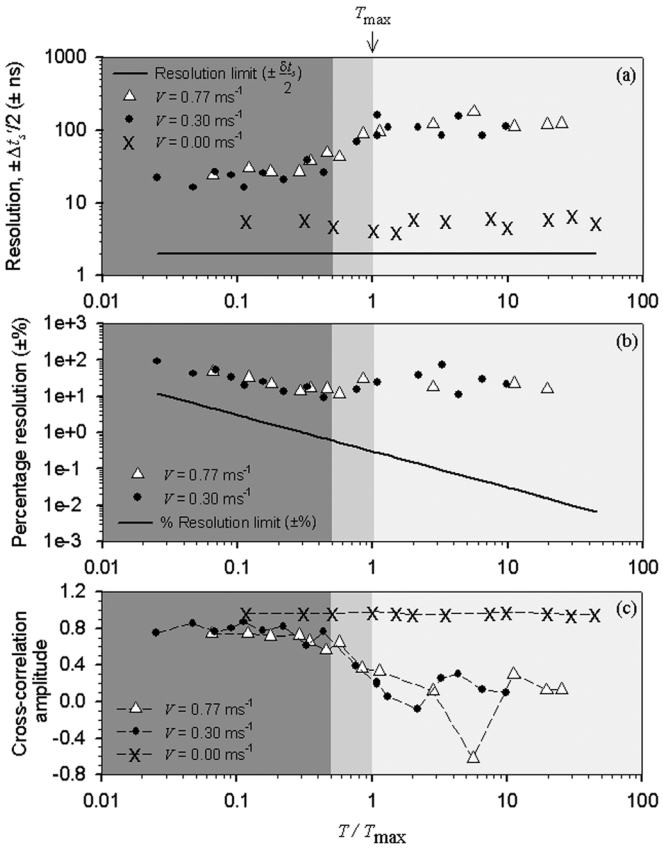

FIG. 10. Resolution and cross-correlation amplitude measured using the 5 MHz focused transducer as a function of relative pulse separation T/T_{max}. (a) Resolution values. The solid line shows the fundamental resolution $\pm\delta t_s/2$ of the system limited by a temporal sampling interval $\delta t_s = 4$ ns. The symbols show the experimentally determined resolution values $\pm\Delta t_s'/2$ [Eq. (9)] for two different velocities; resolution values at zero velocity (invariant with T) are also shown for comparison, arbitrarily setting $T_{max} = 1$ ms. (b) Percentage resolution values for the non-stationary data shown in (a) and for the theoretical limit; percentage resolution for $V = 0.00\,\mathrm{ms}^{-1}$ is undefined (division by zero). (c) Cross-correlation amplitudes for the velocities shown in (a), again setting $T_{max} = 1$ ms for $V = 0.00\,\mathrm{ms}^{-1}$.

The results in Fig. 10 have been used to demonstrate the effects of increasing pulse separation on the experimentally determined resolution of measurements made at fixed velocities. Since the measured time shift is proportional to V as well as T, the general trends observed in Fig. 10 may also be expected in the variation of measurement resolution with increasing velocity (at fixed pulse separation).

Figure 11 illustrates the trends in resolution for the data shown in Fig. 6, where the pulse separation is fixed ($T = 1.5$ ms), and the velocity is varied: the resolution values of the measurements made using the 3.5 MHz, 5 MHz, and 20 MHz transducers are shown for the different values of $|V/V_{max}|$. Figure 11(a) shows the absolute resolution values and in Fig. 11(b) the percentage resolution is shown, relative to the measured velocity values V' [Eq. (16)]. Comparison of the resolution at different velocities with the cross-correlation amplitudes shown in Fig. 11(c) indicates how the resolution is affected by the degree of correlation between waveform pairs. As in Fig. 9, the x axis data have been re-scaled to give the velocity as a proportion of the $|V_{max}|$values.

For $0 \le |V/V_{max}| < 0.5$ (dark grey shading) the measurement resolution [Fig. 11(a)] appears to be relatively consistent (average $\pm 0.02\,\mathrm{ms}^{-1}$ for the 20 MHz transducer, $\pm 0.05\,\mathrm{ms}^{-1}$ for the 5 MHz transducer and $\pm 0.05\,\mathrm{ms}^{-1}$ for the 3.5 MHz transducer), as expected from Eq. (15). The consistency in the absolute resolution means that the percentage resolution improves inversely with increasing velocity, as illustrated in Fig. 11(b), which is comparable to the trend with increasing pulse separation shown in Fig. 10(b). Over this velocity range, the cross-correlation amplitudes [Fig. 11(c)] maintain fairly steady average values of 0.5, 0.6 and 0.9 for the 20 MHz, 5 MHz and 3.5 MHz transducers, respectively. All three data sets exhibit a drop in cross-correlation amplitude over the range $0.5 \le |V/V_{max}| < 1$ (lighter grey shading), as well as decreases in absolute and percentage resolution [Figs. 11(a) and 11(b)]. These changes are explained by the loss of correlation associated with an

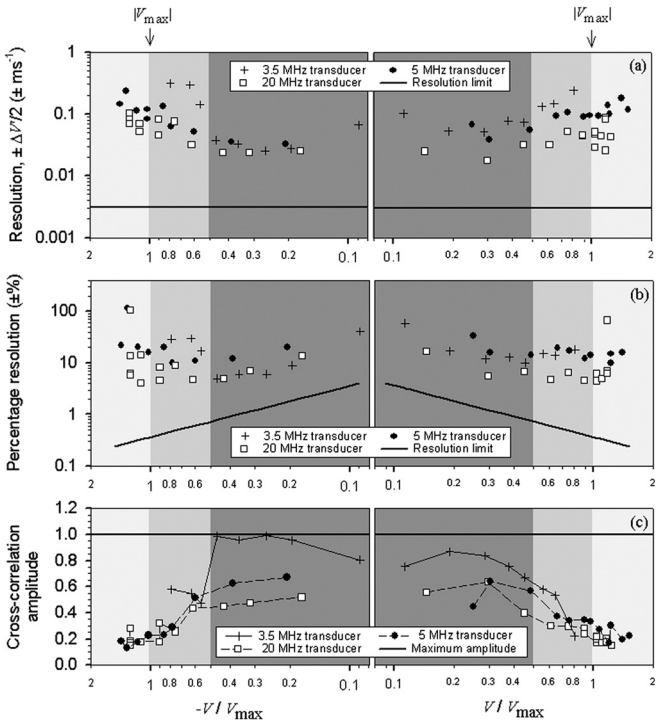

FIG. 11. Resolution and cross-correlation amplitude as a function of $V/V_{\max}$ for the data shown in Fig. 6. (a) Resolution values. The solid line shows the fundamental resolution $\pm\delta V/2$ of the system limited by a temporal sampling interval $\delta t_s = 4$ ns. (b) Percentage resolution values. (c) Cross-correlation amplitudes for the data shown in (a) and (b).

increasing proportion of absorbers moving out of the acoustic focal beam during the time between the two laser pulses; the de-correlation is also exacerbated by the increasingly irregular wheel motion. Beyond $|V_{\max}|$ there is minimal correlation and the measured velocities bear little association with the known values, and therefore the relationship of measurement resolution with measured or known velocity is no longer valid.

Both Figs. 10 and 11 illustrate the competing effects of the increase of time shift and the loss of correlation on resolution. The measurement resolution firstly improves as the time shift becomes increasingly larger compared to the time sampling interval and then, for longer pulse separations, as the absorbers are swept out of the transducer field-of-view, the influence of the loss of correlation begins to dominate and the resolution becomes poorer. The de-correlation effect appears to most notably degrade measurement resolution for pulse separations T greater than about 0.5 $T_{\max}$ (Fig. 10) and for velocities V' greater than about 0.5 $|V_{\max}|$ (Fig. 11); below these thresholds the resolution appears to follow the theoretical inverse trend due to the finite sampling interval. For measurement of a particular velocity, the resolution can therefore be optimized by selecting the pulse separation such that T is as large as possible but still below the 0.5 $T_{\max}$ threshold; this will ensure that the sampling interval effect and the correlation effect are both minimized.

In general, the resolution for all measurements made below $|V_{\max}|$ is expected to scale inversely with transducer frequency. This is because a low detector frequency results in a broad cross-correlation peak and hence a greater uncertainty in the location of the maximum. This behavior is demonstrated in Fig. 11 by the absolute and percentage resolution values for the 5 MHz and 20 MHz transducers, and it is also apparent that the poorest absolute resolution data is that acquired with the 3.5 MHz transducer.

D. Measurement scalability

In this study, pulsed photoacoustic Doppler velocity measurements were limited to the range 0.15 – 1.5 ms^{-1} due to experimental limitations as outlined in Sec. III. However, a key feature of the technique is its scalability, enabling measurement of much lower velocities by appropriate choice of the time separation between the laser pulses.

Theoretical values for maximum measurable velocity $|V_{\max}|$ and minimum detectable velocity (resolution) $\pm\delta V/2$ can be calculated for any pulse separation T using Eq. (11) and Eq. (15), respectively. Figure 12 shows these data plotted for the 5 MHz transducer ($w = 0.97$ mm, $\theta = 45°$, $\delta t_s = 4$ ns) over a range 1.0 ms $\leq T \leq$ 19.5 ms and illustrates how the range of measurable velocities scales with increasing pulse separation. A long pulse separation improves measurement resolution by reducing the influence of the finite temporal sampling interval δt_s. For example, a maximum velocity of nearly 0.7 ms^{-1} is measurable using a pulse separation of 2 ms, which also gives a resolution of ± 2 mms^{-1}. Increasing the pulse separation to 8 ms would reduce $|V_{\max}|$ by a factor of 4 to 0.17 ms^{-1}, but the resolution would improve correspondingly, allowing measurement of velocities down to ± 0.5 mms^{-1}. From the graph and the equations, it is evident that the ratio between $|V_{\max}|$ and $\pm\delta V/2$ remains constant for all pulse separations.

In practice, as seen in Fig. 10 and Fig. 11, the minimum detectable velocity $\pm\Delta V'/2$ obtained experimentally is worse than the theoretical limit $\pm\delta V/2$ by at least a factor of 5. This discrepancy is chiefly a result of de-correlation caused by absorbers moving out of the transducer focal beam; however, for pulse separations below 0.5 $T_{\max}$ the de-correlation

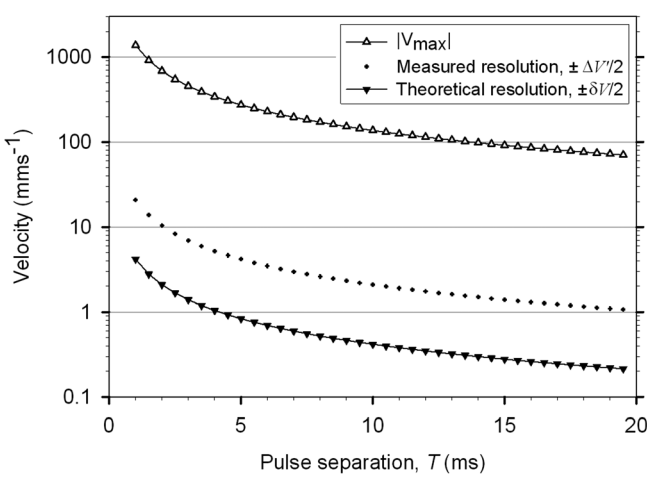

FIG. 12. Scaling of theoretical resolution $\pm\delta V/2$, measured resolution $\pm\Delta V'/2$ (assuming $T < 0.5\ T_{\max}$) and maximum measurable velocity $V_{\max}$ with increasing pulse separation T. The values are calculated based on the 5 MHz transducer ($w = 0.97$ mm) with $\theta = 45°$, and a sampling interval $\delta t_s = 4$ ns.

effect is sufficiently small such that the measurement resolution values still follow the theoretical inverse trend defined by the finite sampling interval. To reflect the discrepancy between the theoretical and experimental resolution values, and provide a realistic indication of the practically achievable resolution, values of $5 \times \delta V/2$ are also plotted in Fig. 12 to represent the measured values $\pm\Delta V'/2$. These reflect the variation of the resolution with pulse duration that can be expected to be achieved in practice using the 5 MHz transducer. These values suggest that pulse separations of $T \geq 20$ ms are required to attain a measurement resolution of ± 1 mms^{-1}. However, adjustment of other experimental factors (for example, increasing the detector bandwidth) could improve the measurement resolution values $\pm\Delta V'/2$ and push them closer to the theoretical limit $\pm\delta V/2$.

E. Spatial resolution

The spatial resolution of the velocity measurements can be defined in lateral and axial directions relative to the axis of the transducer receive beam. The lateral spatial resolution is defined by the FWHM beam width of the transducer (w in Fig. 7), whereas the axial spatial resolution is determined by the length of the range gate (D in Fig. 1). The effect of the axial spatial resolution on the accuracy and resolution of the velocity measurements was investigated by sequentially reducing the range gate applied to FastFrame data sets (25 waveform pairs), which is equivalent to progressively increasing the axial resolution. This is the resolution that would be achieved in the case where absorbers are distributed along the transducer axis, even though the wheel phantom used in this study was confined to a single depth.

Figure 13 shows the results for one FastFrame data set of 25 waveform pairs obtained using the 5 MHz transducer with the wheel phantom moving at a velocity of 0.86 V_{max}. The percentage velocity resolution and cross-correlation amplitude were computed for different range gates. The results were then plotted as a function of the ratio of the axial resolution (defined by the range gate) to the lateral resolution (defined by the FWHM beam width). As the range gate is reduced relative to the beam width the velocity resolution initially improves and there is a corresponding increase in the cross-correlation amplitude. This behavior is due to rejection of the un-correlated data existing in the extremities of the range gate where there is no PA signal; the proportion of correlated data within the range gate is thereby increased. However, as the range gate is reduced further, the two spatial resolution values become comparable (range gate: transducer beam width $\rightarrow$ 1) and the velocity resolution and cross-correlation amplitude deteriorate; this is due to over-restriction of the range gate leading to rejection of correlated parts of the signals arising from absorbers lying in the extremities of the transducer beam profile (i.e. regions just outside the FWHM beam width), but which are nonetheless still sensitive to PA signals. When the range gate is smaller than the transducer beam width it becomes the limiting factor for $|V_{max}|$. In this example, the phantom is moving at a velocity of 0.86 V_{max}, which means that the absorbers traverse 86% of the transducer beam width in the interval between the two illumination pulses. Therefore, once the range gate becomes less than 86% of the transducer beam width (dashed line in Fig. 13) there is no correlation between the waveform pairs. This gives rise to a dramatic increase in fractional error and an associated increase in percentage velocity resolution.

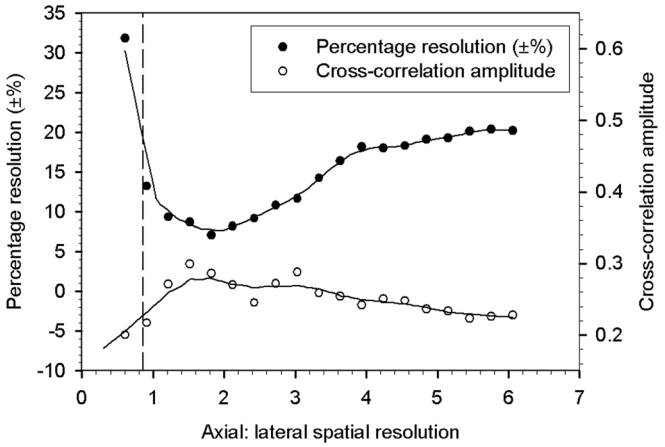

FIG. 13. Variation of velocity resolution and cross-correlation amplitude with the ratio of axial to lateral spatial resolution. Acquisition with the 5 MHz transducer defines the beam width (lateral spatial resolution) to be 0.97 mm, and the length of the range gate (axial resolution) was varied from 6.0 to 0.6 mm. The data points are derived from one measurement, which is plotted in Fig. 6(b), for which the velocity was $V = -0.68$ ms^{-1} (0.86 V_{max}). Correlation is lost for axial: lateral spatial resolution ratios to the left of the dashed line at 0.86.

VI. CONCLUSION

This study has demonstrated that the velocity of a random distribution of micron-scale absorbers can be accurately estimated from time shift measurements obtained by cross-correlation signal processing of photoacoustic waveforms. Using a tissue phantom in which the absorber size and distribution were comparable to those of red blood cells, it has been shown that velocities up to 1.4 ms^{-1} can be accurately measured with a resolution of ± 0.008 ms^{-1} using a laser pulse separation of 1.5 ms. Although photoacoustic Doppler flowmetry is targeted at measuring the much lower flow velocities encountered in the microvasculature (< 50 mms^{-1}), the technique is scalable as discussed in Sec. V D. For example, increasing the pulse separation to 15 ms would, theoretically, allow velocities up to a maximum of 140 mms^{-1} to be measured with a resolution of ± 0.8 mms^{-1}.

Several conclusions in relation to the maximum measurable velocity, accuracy and resolution can be drawn. Firstly, the maximum velocity is defined by the time taken for the absorbers to traverse the transducer focal beam. This upper limit is a function of the pulse separation and transducer beam width—a predictable and well known result from time correlation ultrasound flowmetry.[15] For measurements made at velocities below the upper limit, a high level of quantitative accuracy ($< 1\%$) has been demonstrated. The velocity resolution is at best less than 4% of the measured value, and moreover could be improved by increasing the transducer bandwidth and/or center

frequency. This is evidenced in Fig. 11 where the mean absolute and percentage resolution values obtained using the 5 MHz transducer (bandwidth 2.25 MHz) are 2–3 times poorer than the respective values acquired using the 20 MHz transducer (13 MHz bandwidth). Band limiting either by the transducer or by frequency dependent acoustic attenuation in tissue may be limiting factors in practice, but the former could be addressed, for example by using a broadband high frequency transducer such as one fabricated using PVDF. Other potential limitations include those associated with the nature of fluid flow within a blood vessel. Under the ideal conditions presented by the disc phantom in this study, the movement of the absorbers is unidirectional and the degrading effect of de-correlation on measurement resolution can be minimized using pulse separations $T < 0.5\ T_{\max}$. However, within a blood vessel, the lateral as well as axial movement of RBCs may cause correlation to be lost more rapidly than in the ideal case, necessitating shorter pulse separations and a lowering of the $0.5\ T_{\max}$ threshold. In terms of spatial resolution, the lateral resolution of the velocity measurements is determined by the transducer beam width, whilst the axial spatial resolution depends on the length of the range gate. Figure 13 suggests that the velocity resolution may be optimized using a range gate slightly larger than the transducer beam width.

In this study, emphasis has been placed on demonstrating the underlying measurement principles using a single ultrasound receiver. In practice, however, it is envisaged that the technique would be implemented using an array based photoacoustic imaging system operated in a similar fashion to a conventional combined B-mode/Doppler ultrasound scanner. Thus, an anatomical photoacoustic image of the vasculature would be acquired in the usual way. The velocity could then be obtained at a specific user defined spatial point by synthesizing an appropriate receive beam using the detector array. Since θ is available from the anatomical image and the receive beam direction, absolute velocity measurements can be made. Alternatively, the use of multi-dimensional cross-correlation could be employed to obtain parametric images relating to flow in a manner analogous to conventional color flow ultrasound imaging.

In summary, it is considered that the time correlation photoacoustic method described in this study has potential for measuring blood flow in the microvasculature. Its distinguishing advantages are high spatial resolution, a high degree of scalability in terms of measurement resolution and upper limit of detection, the ability to use the type of Q-switched excitation lasers routinely used in biomedical photoacoustic imaging and the potential for use in acoustic as well as optical resolution photoacoustic sensing modes. It also does not suffer from aliasing which can limit the maximum measurable velocity of other schemes, nor is there any need for calibration in order to obtain absolute velocity measurements. Although the size and distribution of the absorbers in the tissue phantoms used in this study were comparable to those of red blood cells, the acid test of this, and other photoacoustic Doppler flowmetry techniques, is whether they are able to measure the flow of whole blood in the acoustic resolution photoacoustic modes. Demonstrating this will form the subject of future work.

ACKNOWLEDGMENTS

The authors would like to thank Terence Leung for his assistance with the signal processing and Edward Zhang for his contributions to the experimental arrangements.

[1]P. Beard, "Biomedical photoacoustic imaging," Interface Focus **1**, 602–631 (2011).
[2]J. Laufer, P. Johnson, E. Zhang, B. Treeby, B. Cox, B. Pedley, and P. Beard, "In vivo preclinical photoacoustic imaging of tumor vasculature development and therapy," J. Biomed. Opt. **17**, 056016 (2012).
[3]E. Z. Zhang, B. Povazay, J. Laufer, A. Alex, B. Hofer, B. Pedley, C. Glittenberg, B. Treeby, B. Cox, P. Beard, and W. Drexler, "Multimodal photoacoustic and optical coherence tomography scanner using an all optical detection scheme for 3D morphological skin imaging," Biomed. Opt. Express **2**, 2202–2215 (2011).
[4]H. F. Zhang, K. Maslov, G. Stoica, and L. V. Wang, "Functional photoacoustic microscopy for high-resolution and noninvasive in vivo imaging," Nat. Biotechnol. **24**, 848–851 (2006).
[5]J. Laufer, D. Delpy, C. Elwell, and P. Beard, "Quantitative spatially resolved measurement of tissue chromophore concentrations using photoacoustic spectroscopy: Application to the measurement of blood oxygenation and haemoglobin concentration," Phys. Med. Biol. **52**, 141–168 (2007).
[6]P. C. Beard, "Flow velocity measurements," UK Patent Application WO 03/039364 (2001).
[7]H. Fang, K. Maslov, and L. V. Wang, "Photoacoustic doppler effect from flowing small light-absorbing particles," Phys. Rev. Lett. **99**, 184501 (2007).
[8]A. Sheinfeld, S. Gilead, and A. Eyal, "Simultaneous spatial and spectral mapping of flow using photoacoustic Doppler measurement," J. Biomed. Opt. **15**, 066010 (2010).
[9]J. Yao, K. Maslov, Y. Shi, L. Taber, and L. Wang, "In vivo photoacoustic imaging of transverse blood flow by using Doppler broadening of bandwidth," Opt. Lett. **35**, 1419–1421 (2010).
[10]D. H. Evans and W. N. McDicken, *Doppler Ultrasound: Physics, Instrumentation, and Signal Processing*, 2nd ed. (Wiley, Chichester, 2000), pp. 229–284.
[11]C. Kasai, A. Harada, and K. Namekawa, "Real-time blood-flow imaging system using ultrasonic Doppler techniques," Syst. Comp. Jpn. **19**, 13–24 (1988).
[12]J. Yao, K. I. Maslov, Y. Zhang, Y. Xia, and L. V. Wang, "Label-free oxygen-metabolic photoacoustic microscopy in vivo," J. Biomed. Optics **16**, 076003 (2011).
[13]S.-L. Chen, Z. Xie, P. L. Carson, X. Wang, and L. J. Guo, "In vivo flow speed measurement of capillaries by photoacoustic correlation spectroscopy," Opt. Lett. **36**, 4017–4019 (2011).
[14]O. Bonnefous and P. Pesque, "Time domain formulation of pulse-Doppler ultrasound and blood velocity estimation by cross correlation," Ultrasonic Imaging **85**, 73–85 (1986).
[15]I. A. Hein and W. R. O'Brien, "Current time-domain methods for assessing tissue motion by analysis from reflected ultrasound echoes—A review," IEEE Trans. Ultrason. Ferroelectr. Freq. Control, **40**, 84–102 (1993).
[16]J. Brunker and P. Beard, "Pulsed photoacoustic Doppler flowmetry using a cross correlation method" in *Proc. SPIE Int. Soc. Opt. Eng.*, pp. 756426 (2010).
[17]J. Brunker and P. Beard, "Pulsed photoacoustic Doppler flow measurements in blood-mimicking phantoms" in *Proc. SPIE Int. Soc. Opt. Eng.*, p. 78991K (2011).
[18]M. Sarimollaoglu, D. A. Nedosekin, Y. Simanovsky, E. I. Galanzha, and V. P. Zharov, "In vivo photoacoustic time-of-flight velocity measurement of single cells and nanoparticles," Opt. Lett. **36**, 4086–4088 (2011).
[19]Analysis of Sensory-Motor Control Performance" in *The Biomedical Engineering Handbook*, 2nd ed., edited by J. Bronzino (CRC Press, 2000), p. 149:17.
[20]Observations of sections from healthy tissue," University of Cambridge, Department of Pathology, (Last viewed 20 December 2011).
[21]B. J. Bain, "Morphology of Blood Cells" in *Blood Cells: A Practical Guide*, 3rd ed. (Wiley-Blackwell, 2002), pp. 52–154.